Research
Materials Genome Engineering—Article

Two-Layer High-Throughput: Effective Mass Calculations Including Warping

Andrew Supka [a], Nicholas A. Mecholsky [b], Marco Buongiorno Nardelli [c,d], Stefano Curtarolo [d,e], Marco Fornari [a,d,*]

[a] Department of Physics & Science of Advanced Materials Program, Central Michigan University, Mount Pleasant, MI 48859, USA
[b] Department of Physics & Vitreous State Laboratory, The Catholic University of America, Washington, DC 20064, USA
[c] Department of Physics & Department of Chemistry, University of North Texas, Denton, TX 76203, USA
[d] Center for Autonomous Materials Design, Duke University, Durham, NC 27708, USA
[e] Department of Mechanical Engineering and Materials Science, Duke University, Durham, NC 27708, USA

ABSTRACT

In this paper, we perform two-layer high-throughput calculations. In the first layer, which involves changing the crystal structure and/or chemical composition, we analyze selected III–V semiconductors, filled and unfilled skutterudites, as well as rock salt and layered chalcogenides. The second layer searches the full Brillouin zone (BZ) for critical points within 1.5 eV (1 eV = 1.602176 × 10⁻¹⁹ J) of the Fermi level and characterizes those points by computing the effective masses. We introduce several methods to compute the effective masses from first principles and compare them to each other. Our approach also includes the calculation of the density-of-states effective masses for warped critical points, where traditional approaches fail to give consistent results due to an underlying non-analytic behavior of the critical point. We demonstrate the need to consider the band structure in its full complexity and the value of complementary approaches to compute the effective masses. We also provide computational evidence that warping occurs only in the presence of degeneracies.

© 2022 THE AUTHORS. Published by Elsevier LTD on behalf of Chinese Academy of Engineering and Higher Education Press Limited Company. This is an open access article under the CC BY-NC-ND license (http://creativecommons.org/licenses/by-nc-nd/4.0/).

1. Introduction

The electronic band structure plays a fundamental role in our understanding of the origins of the physical properties of materials and in assessing paths for optimization and chemical substitutions. The dispersion relation of the solutions of the many-body electronic Schrödinger equation provides quantitative information that is essential for understanding most of the functionalities that a material may exhibit. The band structure, $E_n(\boldsymbol{k})$, is a mapping from $\mathbb{R}^3 \rightarrow \mathbb{R}^N$ (where N is the number of relevant bands, n is the band index, and $\boldsymbol{k}$ is a vector indicating the crystalline momentum) and is usually represented by considering only two-dimensional (2D) band plots. Because any given band is a function whose domain is the three-dimensional (3D) Brillouin zone (BZ), $\boldsymbol{k} \in \mathrm{BZ} \subset \mathbb{R}^3$, the graph of a given band is embedded in four dimensions. Band structure plots along high-symmetry lines are a useful tool for evaluating a material at a glance. However, the 2D representation hides the full complexity of the electronic spectrum by ignoring large sections of the BZ. Conventions, such as those in Ref. [1], provide common ground for band plots, but 2D band representations are intrinsically limited.

Critical points, where $\partial E_n(\boldsymbol{k})/\partial \boldsymbol{k} = 0$ (with $\partial E_n(\boldsymbol{k})/\partial \boldsymbol{k}$ indicating the gradient of $E_n(\boldsymbol{k})$ with respect to $\boldsymbol{k}$), are an important feature of the electronic band structure. At these points, the density of states (DOS; also represented by the function of energy E, $D(E)$) is large (or diverges; see Ref. [2]):

$$D(E) = 2\sum_n \int_{E_n(\boldsymbol{k})\equiv E} \frac{V}{(2\pi)^3} \frac{\mathrm{d}S}{|\partial E_n(\boldsymbol{k})/\partial \boldsymbol{k}|} \tag{1}$$

with the unit cell volume V and an infinitesimal element of the constant energy surface dS. Critical points are key in evaluating a material's physical properties and fully characterizing the material. For example, for a 2D material, it is well known that saddle points lead to logarithmic singularities [3], and that maxima and minima in three dimensions lead to square root dependencies of the DOS

and, in general, to van Hove singularities or non-smooth points [4]. Thus, the identification of all critical points is an important goal.

A related concept associated with the local properties of the electronic band structure involves the effective mass tensor $\mathbf{M}^*$, which is—assuming Taylor expansibility near $\mathbf{k}_0$—a second-rank tensor in 3D with components:

$$\mathbf{M}^*_{n,ij}(\mathbf{k}_0) = \frac{\hbar^2}{m_e}\left(\frac{\partial^2 E_n(\mathbf{k})}{\partial k_i \partial k_j}\right)^{-1}_{\mathbf{k}_0} \tag{2}$$

where n is the band index, $\hbar$ is the reduced Planck constant, m_e is the mass of electron, and the subscripts i, j are used to label the Cartesian components of the tensor $\mathbf{M}^*$ or of the vector $\mathbf{k}$. The reciprocal of the effective mass tensor is associated with the curvature of the energy dispersion, $E_n(\mathbf{k})$, and is a critical descriptor when discussing electronic transport and optical properties; its evaluation must be done by considering the full mathematical complexity of the band structure. In addition, the possible presence of non-analytic points—such as points where the Hessian is not a symmetric matrix—leads to warped critical points, which play a role in several situations [5,6] but are difficult to identify with 2D band plots. By determining high-fidelity effective mass tensors at critical points, it is possible to formulate analytic models of band structures. Such models are important in many considerations in solid-state physics and electronic engineering; for example, they can be used as a starting point for Monte Carlo transport simulations [7] or for the multi-scale modeling [8] of electronic devices, batteries, and thermoelectric energy converters. Analytic band structures are used in applications such as modeling scattering rates where derivatives and integrals of the bands are necessary [7]. From an experimental standpoint, the DOS effective mass is a common property of the band structure that may be measured through cyclotron resonance [9–18], the four coefficients method [19], Shubnikov–de Haas oscillations [16,20–23], magnetophonon resonance [15,16,24,25], time-of-flight drift velocity [7,26–29], optical transmission and reflection [30–32], and infrared reflection and Faraday rotation [33–35]. Being able to compare the different measurements of the effective mass obtained with those indirect methods and reconcile such results with electronic structure calculations is a major goal.

This paper introduces a two-layer high-throughput (HT) methodology with the aim of partially addressing the misalignment between theory and experiment in the current literature. The first layer is a conventional chemical substitution/structural variation (e.g., see Refs. [36–42]), and the second is a careful exploration of $E_n(\mathbf{k})$ to identify the nature of the critical points and compute the effective mass tensors. The conventional HT considers an array of prototypical materials: III–V semiconductors, filled and unfilled skutterudites, as well as rock salt and layered chalcogenides. For each material, we search the full BZ for critical points and determine the effective mass at those points using several different methodologies for verification [43]. These methodologies also characterize the warping of bands and correctly compute the DOS effective mass at those warped points [6]. To our knowledge, this is the first HT calculation of effective masses in a large portion of the BZ.

In Section 2, we illustrate the details of the computations. Section 3 presents selected results (a large part of the data is included in Appendix A), and Section 4 discusses the impact of this work.

2. Methods

The prototypical materials selected for this work are as follows: III–V semiconductors (AlSb and AlP with the zincblende structure); rock salt (PbTe, GeTe, SnTe, PbS, GeS, SnS, PbSe, GeSe, and SnSe)

and layered chalcogenides (Bi_2Te_3, Bi_2Te_2Se, Bi_2Se_2Te, Bi_2Se_3, Bi_2Te_2S, and Bi_2Se_2S); and pristine and fully filled cobalt antimonide (specifically $CoSb_3$, $CaCo_4Sb_{12}$, and $BaCo_4Sb_{12}$). For each material, the workflow starts by generating a projected atomic orbital tight-binding (PAO-TB) Hamiltonian, which is exploited to interpolate the band structure efficiently and precisely [44]. We use Quantum Espresso (Quantum ESPRESSO Foundation, UK) [45,46] to calculate the electronic structure in the AFLOWπ HT computational framework [47].

The AFLOWπ's workflow (Fig. 1) drives the calculation of the Hubbard U correction within the ACBN0 [48–51] scheme (see Tables S1, S4, S14, and S18 in Appendix A), optimizes the structure of the unit cell, and generates the PAO-TB Hamiltonian. The wavefunction and charge kinetic energy cutoffs were 150 and 600 Ry (1 Ry = 2.179872 × 10^{-18} J), respectively, and a Monkhorst–Pack $\mathbf{k}$-point grid with a density of about 0.01 Å^{-1} has been used. The choice of pseudopotentials was driven by a need to maximize the number of well-projected bands in the PAO-TB model; for this purpose, Perdew–Burke–Ernzerhof (PBE)-projector augmented wave (PAW) pseudopotentials generated from the PSlibrary [52] were modified to have an extended basis [44]. The computations included spin–orbit coupling. For comparison and testing of warping, calculations without spin–orbit were also performed. PAOFLOW (University of North Texas, USA) [53] was used to project the computationally expensive Hamiltonian from the plane wave basis into the more efficient PAO-TB basis. The PAO-TB Hamiltonian allows the exploitation of the Fourier interpolation to obtain a smooth version of the band structure. The full BZ was divided into a 12 × 12 × 12 grid, and each voxel was searched for

```
import AFLOWpi
import glob

# start the AFLOWpi with config file AFLOWpi.config
session = AFLOWpi.prep.init('WARPING', SET='Warp_HT',
                            config='./AFLOWpi.config')
# get a list of QE input files
input_files = glob.glob('./ input_files /*.in')
# form the calculation set from list of input files
calcs = session.scfs ( input_files )
# relax the structure
calcs.vcrelax()
# perform self–consistent Hubbard U calculation
calcs.acbn0(kp_factor=2)
# relax the structure with Hubbard U
calcs.vcrelax()
# change to fully relativistic pseudopotentials
calcs.change_pseudos(".//FR_PP/")
# set spin orbit flag to true
calcs.change_input("&system","lspinorb",".true.")
calcs.change_input("&system","noncolin",".true.")
calcs.change_input("&system","lda_plus_u_kind","1")
# calculate tight binding Hamiltonian
calcs_tb=calcs.tight_binding(kp_factor=2,proj_thr=0.99)
# calculate band structure and density
# of states using PAO–TB Hamiltonian
calcs_tb.dos()
calcs_tb.bands()
# plot band structure and density of states
calcs_tb.plot.bands(en_range=[–5,5])
calcs_tb.plot.dos(en_range=[–5,5])
# make sure the os package is loaded
calcs.addToAll('POSTPROCESSING','import os')
# string of command to run after PAO–TB Hamiltonian generated
wppc = "os.system('srun –n 56 python ~/warp_pp.py > warp.out')"
# add command to run the warping code as post–
# processing to all of the calculations in the set
calcs.addToAll("POSTPROCESSING",wppc))
# submit calculations to queue
calcs.submit()
```

Fig. 1. The AFLOWπ workflow script used in this study. More details on AFLOWπ are available in Ref. [47].

an isolated critical point. It was assumed that a voxel would contain at most one critical point. We chose a $12 \times 12 \times 12$ grid to strike a balance between accuracy and computational efficiency. The locations of the critical points in $\boldsymbol{k}$-space were then compared using operations of the symmetry group to identify unique critical points. This was done for ease of computation and for uniformity in analysis, given different crystal structures.

In order to identify critical points, we identified $\boldsymbol{k}$-points, where the band velocities $\boldsymbol{v}_n$ are very small.

$$\left| \frac{1}{\hbar} \frac{\partial E_n(\boldsymbol{k})}{\partial \boldsymbol{k}} \right| = \boldsymbol{v}_n(\boldsymbol{k}) < \frac{1}{\hbar} \times 10^{-8} \frac{eV}{a_B} \tag{3}$$

Fig. 2 shows a typical case of a saddle point for SnTe. The three panels show the three components of the velocity $\boldsymbol{v}$. The electron group velocity was calculated via the PAO-TB Hamiltonian by taking the expectation value of the momentum operator $\boldsymbol{p}$, as discussed in Ref. [2]

$$\boldsymbol{v}_n(\boldsymbol{k}) = \frac{1}{\hbar} \langle \psi_n(\boldsymbol{k}) \left| \frac{\boldsymbol{p}}{m_e} \right| \psi_n(\boldsymbol{k}) \rangle \propto \langle \psi_n(\boldsymbol{k}) \left| \frac{\partial \boldsymbol{H}(\boldsymbol{k})}{\partial \boldsymbol{k}} \right| \psi_n(\boldsymbol{k}) \rangle \tag{4}$$

where $\boldsymbol{H}$ is the Hamiltonian and ψ_n is the single-particle wavefunction.

Starting from the energy dispersion, we computed the Hessian matrix using second-order Fourier derivatives [54,55]:

$$\frac{\partial^2 E_n(\boldsymbol{k})}{\partial k_i \partial k_j} = \langle \psi_n(\boldsymbol{k}) \left| \frac{\partial^2 \boldsymbol{H}(\boldsymbol{k})}{\partial k_i \partial k_j} \right| \psi_n(\boldsymbol{k}) \rangle + 2 \langle \frac{\psi_n(\boldsymbol{k})}{\partial k_i} \left| \frac{\partial \boldsymbol{H}(\boldsymbol{k})}{\partial k_j} \right| \psi_n(\boldsymbol{k}) \rangle \tag{5}$$

The inverse of the Hessian matrix is proportional to the effective mass tensor in the chosen reference system. Diagonalization of $\boldsymbol{M}^*$ leads to the three eigenvalues m_1, m_2, and m_3. The DOS effective mass is calculated by taking the geometric mean of the three effective mass components, m_1, m_2, and m_3:

$$m_{\text{DOS}}^* = (m_1 m_2 m_3)^{\frac{1}{3}} = (\det \boldsymbol{M}^*)^{\frac{1}{3}} \tag{6}$$

It should be noted that, in the definition of m_{DOS}^*, only one among the possible equivalent $\boldsymbol{k}$-points is considered. The validity of the Fourier approach (which is very efficient computationally) holds for all non-warped bands but fails in the case of warped bands where the Hessian is not symmetric. In order to treat all the critical points in the same way, we calculated the inverse effective mass surface (IEMS) and used it to determine the three diagonal components of the effective mass tensor, the DOS effective mass accounting for band warping effects [6], and the band warping parameter (w) [5].

The IEMS was generated by interpolating the energy dispersion using a radial grid centered on each critical point. For each critical point and each angular direction in the spherical grid (defined by φ, θ), we found the second derivative of the energy dispersion along the radial direction k_r—that gives, the effective mass in a given radial direction (Fig. 3) near $E_n(\boldsymbol{k}_0) = E_{n0}$. The band curvature $\partial^2 E / \partial k_r^2$ gives the second-order coefficient, $f_2(\varphi, \theta)$, in the radial one-dimensional (1D) Taylor expansion (in natural units):

$$E_n(k_r, \varphi, \theta) = E_{n0} + f_1(\varphi, \theta) k_r + \frac{1}{2} f_2(\varphi, \theta) k_r^2 + \cdots \tag{7}$$

This angular form is very general [5] and allows for the treatment of non-analytic (hence warped, non-Taylor series expandable) critical points in the band structure. Similarly to previous work [5,6], we opted to fit our radial energy dispersion to a polynomial function greater than order two in order to account for possible band non-parabolicity, which can be clearly seen in Fig. 3. In order to calculate the three components of the effective mass, the DOS effective mass for warped bands, and the warping parameter, we fitted the values of the IEMS at a given critical point. We chose an expansion in real spherical harmonics to be a general form for future analysis.

$$f_2(\varphi, \theta) = \sum_{l=0}^{30} \sum_{m=-l}^{l} A_{lm} Y_{lm}(\varphi, \theta) \tag{8}$$

The basis of real spherical harmonics, $Y_{lm}(\varphi, \theta)$ includes the Condon–Shortley phase [56]. For analytic critical points, the diagonal form of the inverse effective mass tensor, $(m_1^{-1}, m_2^{-1}, m_3^{-1})$, was found by aligning a set of orthogonal axes with the maximal values of the IEMS. Fitting the surface in these coordinates to the simplified form, as shown in Eq. (9), gives the effective masses directly [5,6].

$$f_2(\varphi, \theta) = \frac{\cos^2 \theta}{m_3} + \frac{1}{m_1 m_2} \sin^2 \theta \left(m_2 \cos^2 \varphi + m_1 \sin^2 \varphi \right) \tag{9}$$

The direction of the maximal values of the IEMS aligns with the principal axes of the ellipsoids of constant energy and corresponds to a coordinate system in which the inverse effective mass tensor is diagonal. In general, the IEMS near an analytic critical point is a quadratic form:

$$f_2(\varphi, \theta) = \hat{\boldsymbol{k}} \cdot \boldsymbol{H} \cdot \hat{\boldsymbol{k}} \tag{10}$$

where

$$\boldsymbol{H} = \boldsymbol{A}^{\text{T}} \cdot \begin{pmatrix} m_1^{-1} & 0 & 0 \\ 0 & m_2^{-1} & 0 \\ 0 & 0 & m_3^{-1} \end{pmatrix} \cdot \boldsymbol{A} \tag{11}$$

is the matrix of second partial derivatives of the energy dispersion and $\boldsymbol{A}$ is the Euler rotation matrix (see Eq. 4.46 in Ref. [57]). Here,
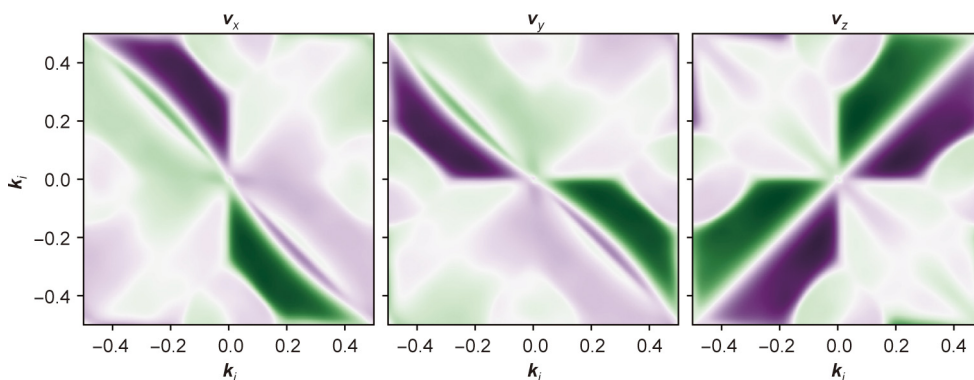

Fig. 2. A 2D slice $\boldsymbol{k} = (i, j, 0.5)$ of the 3 components of the gradient of the energy for the bottom conduction band in the first BZ for SnTe. The purple and green represent $\boldsymbol{k}$ with large positive and negative values, respectively, for each gradient component.
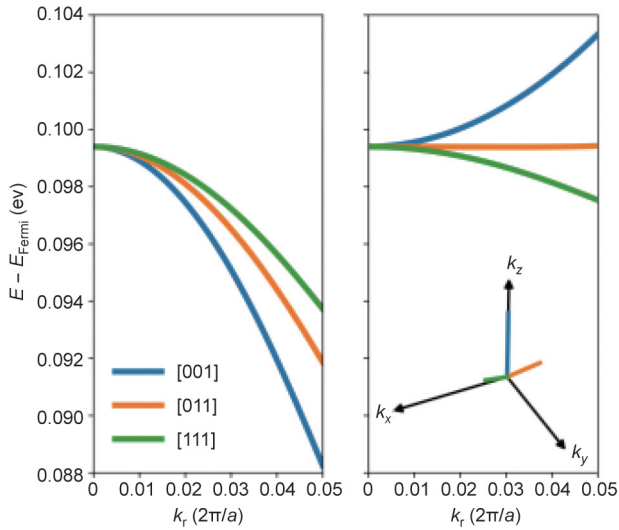
Fig. 3. Energy dispersion in several radial directions around the degenerate, warped Γ point $\boldsymbol{k} = (0, 0, 0)$ near the Fermi level (E_{Fermi}) in CaCo$_4$Sb$_{12}$. The lattice parameter is indicated with a.

$$\hat{\boldsymbol{k}} = (\sin\theta\cos\varphi, \ \sin\theta\sin\varphi, \ \cos\theta) \tag{12}$$

is the angular $\hat{\boldsymbol{k}}$ unit vector. The matrix $\boldsymbol{H}$ may be diagonalized to find the diagonal values (m_1^{-1}, m_2^{-1}, and m_3^{-1}), as well as the directions of the principal axes. Alternatively, if the principal axes can be found first, as described above, the masses may be read off from a fit to Eq. (9). The algorithm is described as follows: Given the standard Cartesian basis X, Y, and Z defined by the coordinate system of the Y_{lm}s, let X', Y', and Z' be the axes after step ①, as defined below, and X'', Y'', and Z'' be the axes transformed from X', Y', and Z' with the transformation in ② below. The procedure can be done by ① finding Euler angles Φ and Θ that rotates the reference Z axis to the direction of the maximum absolute value of the IEMS; and ② with a fixed Φ and Θ from the previous step, rotating the X' axis around the Z' axis until it achieves a maximum value. The third direction is orthogonal to the $Z'' = Z'$ and X'' axes in a right-handed coordinate system. The value of the IEMS along the X'', Y'', and Z'' axes corresponds to m_1^{-1}, m_2^{-1}, and m_3^{-1}, respectively. In the case of non-analytic critical points, the DOS effective mass m_{DOS}^* is computed by integrating a particular function of the IEMS [6] over the entire angular surface at a given point:

$$m_{DOS}^* = \pm\frac{C_\pm}{2\pi} \tag{13}$$

$$C_\pm = \iint \frac{\sin\theta}{2|f_2(\varphi, \ \theta)|^{\frac{3}{2}}}\mathrm{d}\theta\mathrm{d}\varphi \tag{14}$$

The sign of the integral depends on the sign of the IEMS. For saddle points, the value of the integrand in Eq. (14) approaches infinity when $f_2(\varphi, \ \theta)$ approaches zero. In principle, one can integrate over the range of φ and θ where $f_2(\varphi, \ \theta)$ is positive and separately where it is negative. In practice, however, it proves difficult to achieve convergence for the integral, and we do not include the calculation of the DOS effective mass for warped saddle points in our results. To the best of our knowledge, the problem of properly accounting for saddle points is still unsolved.

3. Results

There is a wide range of effects on the DOS and other material properties from the local band structure at critical points [4]. The HT procedure produces many such critical points for a given crystal, and the distribution and type of critical points ultimately account for the similarities and differences in material properties. Table 1 [58,59] summarizes some of our computations for several common materials in comparison with reference values. The effective mass was computed by all three methods discussed above: m_{DOS}^* by fitting Fourier derivatives (Eq. (6), m_F^*), m_{DOS}^* by fitting the IEMS (m_I^*), and m_{DOS}^* from the warped definition (m_w^* evaluated from Eqs. (13) and (14)). It should be noticed that, in Table 1, all calculations for masses agree for non-warped critical points, including the warped calculation of Eqs. (13) and (14). This is to be expected and is reflected in the data in general. Large discrepancies in the experimental effective masses of different materials make it difficult to directly compare with the calculated effective mass; however, our study compares favorably in most cases with the results from previous work (Table 1). All our results are included in Appendix A, specifically the band structure plots, the Hubbard U corrections, and the effective mass computed for critical points in the proximity of the Fermi level. It should be noted that experimental data are not available for critical points away from the Fermi level.

It is found that, overall, there are a considerable number of critical points, and warped critical points are not uncommon. Fig. 4 shows a typical BZ for FCC GeS (included in Table S5 in Appendix A). The plotted shapes display 18 critical point locations. Each critical point also has several symmetry-related neighbors that are determined by the point group at the location of the given critical point. In this case, there are 307 critical points in total, including all symmetries (but discounting critical points at the same $\boldsymbol{k}$ but different energy). We found that 57% of the critical points identified in our search were saddle points that manifest as van Hove singularities in the DOS [3]. In the case of a saddle point, the eigenvalues of $\boldsymbol{M}^*$ have a different sign. The DOS effective mass obtained using Eqs. (13) and (14) diverges for a hyperbolic IEMS and is not calculated. The calculations of the DOS effective mass determined via the fitting procedure and via second-order derivatives are numerically equivalent in cases where band warping does not occur. Where warping occurs (e.g., in Table 2), there is a large difference between the fitting procedure and the Fourier derivative method, since the warping effects prevent the energy from being Taylor expanded in three dimensions. We found that band warping only occurred at critical points with degenerate energy eigenvalues, and we did not find any band

Table 1
Comparison of the IEMS fit (m_I^*), Fourier derivative (m_F^*), and warped (m_w^*) DOS effective masses calculated in our study with measured values (m_{exp}^*). The subscripts indicate the band-type (e: electron, h: hole, so: split-off), L and Γ are the conventional labels for two different critical points.

Sample	Type	m_I^*	m_F^*	m_w^*	m_{exp}^*
PbTe	$m_e^*(L)$	0.105	0.105	0.105	0.13 [58]
PbTe	$m_h^*(L)$	−0.120	−0.120	−0.120	0.13 [58]
AlP	$m_e^*(\Gamma)$	0.235	0.235	0.235	0.22 [59]
AlP	m_{so}^*	−0.346	−0.346	−0.346	0.29–0.34 [59]
AlSb	m_{so}^*	−0.237	−0.237	−0.237	0.22 [59]
AlSb	$m_e^*(\Gamma)$	0.100	0.099	0.100	0.09–0.18 [59]

warping at isolated non-degenerate critical points. Fig. 5 shows an example of the band structure of silicon (Si), with the critical points marked with red points and the degree of warping noted as red disks. The magnitude of the warping parameter is indicated by the diameter of the disk. It can be seen that the valence band is warped, albeit mildly with respect to some of the other critical points, whereas the conduction band minimum along Δ is not warped. Table 2 shows a sample of some representative warped critical points. The warping parameter gives a measure of the degree of warping. With zero warping, the critical point is ellipsoidal or hyperbolic, and the DOS effective masses from the other two methods (m_I^* and m_F^*) agree with the warped calculation (m_w^*). However, it can be seen that the values of the direct fit (m_I^*) and Fourier derivative (m_F^*) method do not agree with each other at warped critical points. This is to be expected, since the fit will depend on the choice of coordinates at a non-analytic point. The failure stems from the fact that the IEMS cannot be fit to an ellipsoidal surface at a warped point. The warping parameter, as defined in Ref. [5], is computed for all critical points and determines whether a fitting procedure to an ellipsoidal form is appropriate.
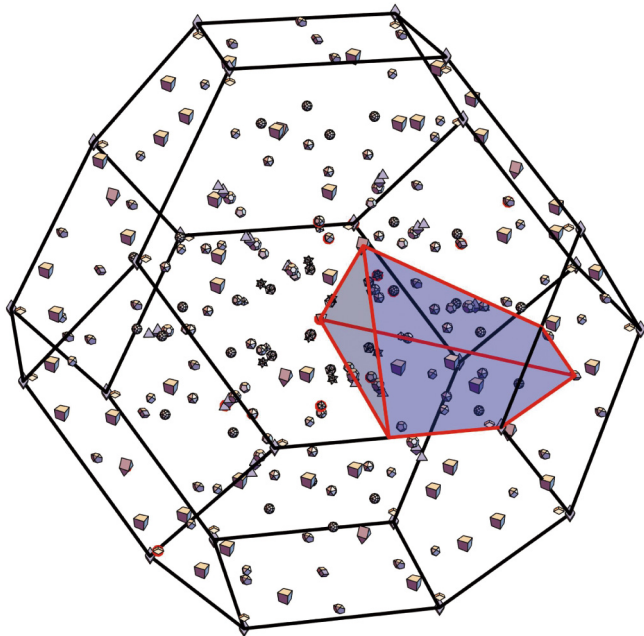
Consider Fig. 6 where the relative error of the direct fitting relative to the warped DOS effective mass is plotted versus the warping parameter. It can be seen from the figure that there is a general positive correlation, indicating that the warping parameter is a measure of how badly traditional methods (e.g., direct fitting or the Fourier method) perform when evaluating effective masses; thus, the warping parameter is an indication of how badly a Taylor approximation will perform in approximating the surface of an IEMS at a warped point. This is similar to what is reported in Ref. [6] for a surface warped in Kittel's form. Thus, the only correct value for the DOS effective mass is m_w^*. Fig. 7 shows the DOS of $CaCo_4Sb_{12}$. Critical points (van Hove singularities) are marked as red disks. The size of the disk indicates the amount of warping, as calculated in Ref. [5]. It can be seen that the DOS effective masses give rise to the shape of the non-smooth points. The particular shape can be expressed in terms of the DOS effective mass [4,6]. With spin–orbit coupling included, the largest warping value w is about 1.94 in $CaCo_4Sb_{12}$ at Γ. In general, without spin–orbit coupling, there are many more warped points (since spin–orbit coupling lifts degeneracy), and the warping is larger in that case. This study provides a computational answer to questions related to the origin and occurrence of warping effects [60]. Without exception, warping did not occur at a specific critical point without the presence of degeneracies.
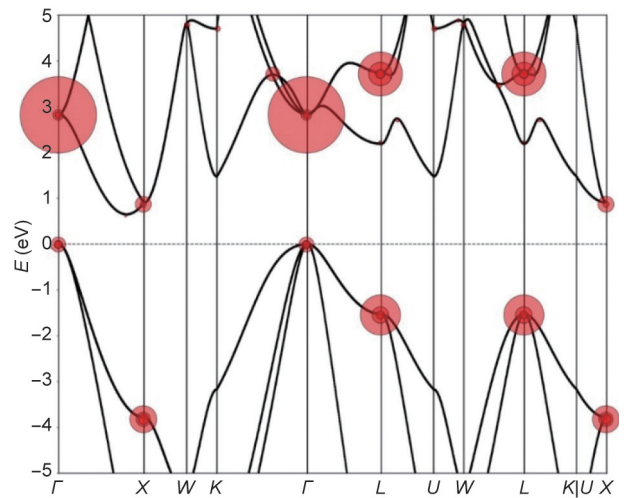

Fig. 4. Critical points for FCC GeS in the first BZ. Each polyhedral shape relates to a different symmetry (star of the **k**-point) of the BZ, depending on the location of a representative point.

Fig. 5. An example of the Si band structure computed along the path suggested by Ref. [1] without spin–orbit coupling and with warping noted in red circles. The magnitude of the warping parameter w, is given as the size of the disk.

Table 2
Warping extent w and DOS effective mass at selected warped critical points calculated with 3 different methods: integral over the IEMS, ellipsoidal fit of the IEMS, and second-order Fourier derivative. The table includes the following critical points: hole band m_e^* (H), heavy-hole band (m_{hh}^*), and light-hole band (m_{lh}^*) at $\Gamma = (0, 0, 0)$, the maximum of the valence band (m_{max}^*) at $X = (1, 0, 0)$ or Γ, and selected saddle point (m_{sad}^*) at Γ.

Sample	Type	$E_n(\boldsymbol{k})$	w	m_w^*	m_I^*	m_F^*
AlSb	$m_{hh}^*(\Gamma)$	0	−0.186	−0.549	−0.193	−0.0950
AlSb	$m_{lh}^*(\Gamma)$	0	−0.036	−0.099	−0.095	−0.1890
AlP	$m_{max}^*(X)$	−2.391	0.101	3.979	2.936	0.5746
$CaCo_4Sb_{12}$	$m_e^*(H)$	−0.027	0.055	0.598	0.517	1.2390
PbTe	$m_{max}^*(\Gamma)$	−1.017	0.138	0.556	0.393	0.4080
PbTe	$m_{sad}^*(\Gamma)$	−1.017	−0.497	—	−0.841	−1.0830
GeTe	$m_{max}^*(\Gamma)$	−1.569	0.097	0.316	0.246	1.0430
GeTe	$m_{sad}^*(\Gamma)$	−1.569	−0.551	—	−0.712	−0.9480

Note: For saddle points, the warped DOS effective mass is unavailable. The fit (m_I^*) and Fourier (m_F^*) methods for computing the components of the effective mass are only valid when the IEMS is not warped (ellipsoidal or hyperboloidal). When the IEMS is warped, then the fit and Fourier method fail and the m^* calculated with those methods differs from the correct value of m_w^*.
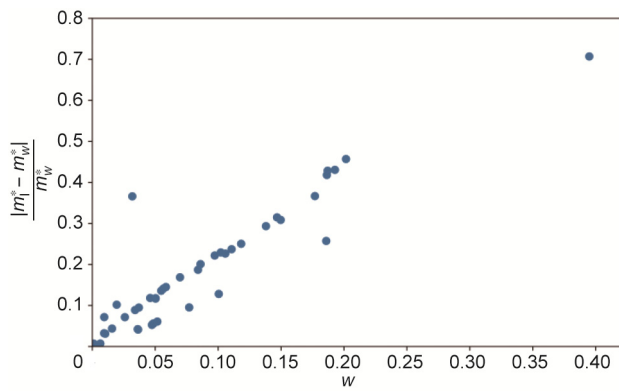
Fig. 6. The error between the warped effective mass DOS calculation and the DOS effective mass calculated with the fit to the IEMS versus the dimensionless warping parameter (w), for the materials in this study.
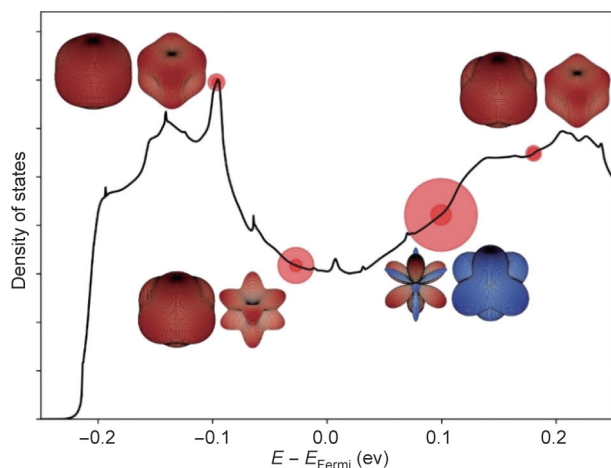

Fig. 7. DOS for $CaCo_4Sb_{12}$ including spin–orbit coupling. The van Hove singularities are identified by red disks, where the diameter of the disk is determined by the warping parameter of the critical point located at the center of the disk. The shapes of the IEMS at the warped critical points are included in the figure. Blue (red) portions of the IEMS represent negative (positive) band curvature.

In all of the cubic materials, all saddle points at Γ and at L (or other critical points) are warped. The reason for this can be seen in the requirements placed on the IEMS: The IEMS will have regions of positive and negative values due to the saddle behavior of the energy dispersion, and the cubic symmetry forces the principal directions to be the same. These two competing geometric requirements lead to warping at these points.

The HT list of critical points and effective masses has a variety of applications. For example, a full approximate analytic model of the BZ may be accomplished by approximating each critical point with the corresponding ellipsoid or saddle in the case of materials where warping is not an issue for critical points near the Fermi energy. This could be used for calculating scattering rates in Monte Carlo simulations [7] or for calculations of relaxation times [61] for different scattering processes. Moreover, a full analytic band structure would allow for possible band engineering, for the exploration of material properties, and even for the low-dimensionality reduction of thermoelectric properties [62]. A full description of the effective masses would also provide a model for the exploration of anisotropic transport considerations. As opposed to critical points that are not near high-symmetry points, lines, or planes, none of the effective masses from a quadratic expansion of the

energy dispersion need to be the same. This gives rise to anisotropic transport that is all but ignored to avoid excessive complication. This procedure provides examples where anisotropy may be relevant for transport or other properties and provides a first step toward realistic analytic descriptions of band structures with these properties.

The Appendix A includes: ① the Hubbard U correction determined with the ACBN0 self-consistent protocol (Tables S1, S4, S14, and S18); ② characterization of the critical points found in the proximity of the Fermi level for AlSb, AlP, GeS, GeSe, GeTe, PbS, PbSe, PbTe, SnS, SnSe, SnTe, $CoSb_3$, $CaCo_4Sb_{12}$, $BaCo_4Sb_{12}$, Bi_2Se_2Te, Bi_2Te_3, Bi_2Te_2Se, Bi_2Se_3, Bi_2Te_2S, and Bi_2Se_2S (Tables S2, S3, S5, S7–S13, S15–S17, and S19–S24 in Appendix A); and ③ band structure plots (Figs. S1–S20 in Appendix A).

4. Conclusions

We have designed and applied a two-level HT calculation with the aim of finding and characterizing critical points in the BZs of several materials. This search identified features of the band structures, $E_n(\mathbf{k})$, that are not visible in 2D plots but nonetheless contribute to electronic transport, DOS, and other material properties. We used three different methods to compute the DOS effective masses at these critical points: namely, the direct method, the Fourier derivative method, and the warped method. At analytic (ellipsoidal) critical points, all approaches agreed with each other and aligned well with literature values, where available. This study also identified many warped critical points and used Eqs. (13) and (14) to correctly calculate the DOS effective mass. At these warped points, we provided reliable values for m^*_{DOS} using the theory reported in Ref. [5]. All three methods disagreed, but the "warped" method was correct. Standard 2D band structure plots are often inadequate to convey the complicated nature of the effective masses at important critical points. Our HT procedure overcomes this issue and facilitates comparison with experiments and the development of analytical models, as well as band structure engineering and the tuning of properties for technological applications.

Compliance with ethics guidelines

Andrew Supka, Nicholas A. Mecholsky, Marco Buongiorno Nardelli, Stefano Curtarolo, and Marco Fornari declare that they have no conflict of interest or financial conflicts to disclose.

Appendix A. Supplementary data

Supplementary data to this article can be found online at https://doi.org/10.1016/j.eng.2021.03.031.

References

[1] Setyawan W, Curtarolo S. High-throughput electronic band structure calculations: challenges and tools. Comput Mater Sci 2010;49(2):299–312.

[2] Grosso G, Parravicini GP. Solid state physics. San Diego: Academic Press; 2000.

[3] Van Hove L. The occurrence of singularities in the elastic frequency distribution of a crystal. Phys Rev 1953;89(6):1189–93.

[4] Bassani F, Parravicini GP. Electronic states and optical transitions in solids. Oxford: Pergamon Press; 1975.

[5] Mecholsky NA, Resca L, Pegg IL, Fornari M. Theory of band warping and its effects on thermoelectronic transport properties. Phys Rev B 2014;89(15):155131.

[6] Mecholsky NA, Resca L, Pegg IL, Fornari M. Density of states for warped energy bands. Sci Rep 2016;6(1):22098.

[7] Jacoboni C, Reggiani L. The Monte Carlo method for the solution of charge transport in semiconductors with applications to covalent materials. Rev Mod Phys 1983;55(3):645–705.

[8] Shi S, Gao J, Liu Y, Zhao Y, Wu Q, Ju W, et al. Multi-scale computation methods: their applications in lithium-ion battery research and development. Chin Phys B 2016;25(1):018212.

[9] Hensel JC, Feher G. Cyclotron resonance experiments in uniaxially stressed silicon: valence band inverse mass parameters and deformation potentials. Phys Rev 1963;129(3):1041–62.

[10] Luttinger JM. Quantum theory of cyclotron resonance in semiconductors: general theory. Phys Rev 1956;102(4):1030–41.

[11] Hasegawa H. Theory of cyclotron resonance in strained silicon crystals. Phys Rev 1963;129(3):1029–40.

[12] Dresselhaus G, Kip AF, Kittel C, Wagoner G. Cyclotron and spin resonance in indium antimonide. Phys Rev 1955;98(2):556–7.

[13] Leotin J, Barbaste R, Askenazy S, Skolnick MS, Stradling RA, Tuchendler J. Hole mass measurement in p-type InP and GaP by submillimetre cyclotron resonance in pulsed magnetic fields. Solid State Commun 1974;15(4):693–7.

[14] Ousset JC, Leotin J, Askenazy S, Skolnick MS, Stradling RA. Cyclotron resonance measurements of the non-parabolicity of the conduction bands in silicon and germanium. J Phys C Solid State Phys 1976;9(14):2803–8.

[15] Sarkar CK, Nicholas RJ, Portal JC, Razeghi M, Chevrier J, Massies J. Effect masses and non-parabolicity in Ga$_x$In$_{1-x}$As. J Phys C Solid State Phys 1985;18(13):2667–76.

[16] Nicholas RJ, Portal JC, Houlbert C, Perrier P, Pearsall TP. An experimental determination of the effective masses for Ga$_x$In$_{1-x}$As$_y$P$_{1-y}$ alloys grown on InP. Appl Phys Lett 1979;34(8):492–4.

[17] Palik ED, Picus GS, Teitler S, Wallis RF. Infrared cyclotron resonance in InSb. Phys Rev 1961;122(2):475–81.

[18] Skolnick MS, Jain AK, Stradling RA, Leotin J, Ousset JC. An investigation of the anisotropy of the valence band of GaAs by cyclotron resonance. J Phys C Solid State Phys 1976;9(14):2809–21.

[19] Young DL, Coutts TJ, Kaydanov VI, Gilmore AS, Mulligan WP. Direct measurement of density-of-states effective mass and scattering parameter in transparent conducting oxides using second-order transport phenomena. J Vac Sci Technol A 2000;18(6):2978–85.

[20] Seiler DG, Stephens AE. The Shubnikov–de Haas effect in semiconductors: a comprehensive review of experimental aspects. In: Seiler DG, editor. Modern problems in condensed matter sciences. Amsterdam: Elsevier Science Publications; 1991. p. 1031–133.

[21] Leadley DR, Nicholas RJ, Foxon CT, Harris JJ. Measurements of the effective mass and scattering times of composite fermions from magnetotransport analysis. Phys Rev Lett 1994;72(12):1906–9.

[22] Restorff JB, Houston B, Burke JR, Hayes RE. Measurement of effective mass in In$_{0.9}$Ga$_{0.1}$As$_{0.22}$P$_{0.78}$ by Shubnikov–de Haas oscillations. Appl Phys Lett 1978;32(3):189–90.

[23] Goiran M, Millot M, Poumirol JM, Gherasoiu I, Walukiewicz W, Leotin J. Electron cyclotron effective mass in indium nitride. Appl Phys Lett 2010;96(5):052117.

[24] Harper PG, Hodby JW, Stradling RA. Electrons and optic phonons in solids—the effects of longitudinal optical lattice vibrations on the electronic excitations of solids. Rep Prog Phys 1973;36(1):1.

[25] Stradling RA, Wood RA. The temperature dependence of the band edge effective masses of InSb, InAs and GaAs as deduced from magnetophonon magnetoresistance measurements. J Phys C Solid State Phys 1970;3(5):L94–9.

[26] Nava F, Canali C, Jacoboni C, Reggiani L, Kozlov SF. Electron effective masses and lattice scattering in natural diamond. Solid State Commun 1980;33(4):475–7.

[27] Canali C, Jacoboni C, Nava F, Ottaviani G, Alberigi-Quaranta A. Electron drift velocity in silicon. Phys Rev B 1975;12(6):2265–84.

[28] Fawcett W, Boardman AD, Swain S. Monte Carlo determination of electron transport properties in gallium arsenide. J Phys Chem Solids 1970;31(9):1963–90.

[29] Fawcett W, Paige EGS. Negative differential mobility of electrons in germanium: a Monte Carlo calculation of the distribution function, drift velocity and carrier population in the (111) and (100) minima. J Phys C Solid State Phys 1971;4(13):1801–21.

[30] Spitzer WG, Fan HY. Determination of optical constants and carrier effective mass of semiconductors. Phys Rev 1957;106(5):882–90.

[31] Spitzer WG, Whelan JM. Infrared absorption and electron effective mass in n-type gallium arsenide. Phys Rev 1959;114(1):59–63.

[32] Weisbuch C, Hermann C. Optical detection of conduction-electron spin resonance in GaAs, Ga$_{1-x}$In$_x$As, and Ga$_{1-x}$Al$_x$As. Phys Rev B 1977;15(2):816–22.

[33] Cardona M, Paul W, Brooks H. The temperature dependence of the polarizability of the free carriers in germanium and silicon. Helv Phys Acta 1960;33:329–46.

[34] Cardona M. Electron effective masses of InAs and GaAs as a function of temperature and doping. Phys Rev 1961;121(3):752–8.

[35] Lyden HA. Measurement of the conductivity effective mass in semiconductors using infrared reflection. Phys Rev 1964;134(4A):A1106–12.

[36] Armiento R, Kozinsky B, Hautier G, Fornari M, Ceder G. High-throughput screening of perovskite alloys for piezoelectric performance and thermodynamic stability. Phys Rev B 2014;89(13):134103.

[37] Armiento R, Kozinsky B, Fornari M, Ceder G. Screening for high-performance piezoelectrics using high-throughput density functional theory. Phys Rev B 2011;84(1):014103.

[38] Mounet N, Gibertini M, Schwaller P, Campi D, Merkys A, Marrazzo A, et al. Two-dimensional materials from high-throughput computational exfoliation of experimentally known compounds. Nat Nanotechnol 2018;13(3):246–52.

[39] Burton LA, Ricci F, Chen W, Rignanese GM, Hautier G. High-throughput identification of electrides from all known inorganic materials. Chem Mater 2018;30(21):7521–6.

[40] Li R, Li X, Xi L, Yang J, Singh DJ, Zhang W. High-throughput screening for advanced thermoelectric materials: diamond-like ABX$_2$ compounds. ACS Appl Mater Interfaces 2019;11(28):24859–66.

[41] Aykol M, Kim S, Hegde VI, Snydacker D, Lu Z, Hao S, et al. High-throughput computational design of cathode coatings for Li-ion batteries. Nat Commun 2016;7(1):13779.

[42] Zhu H, Hautier G, Aydemir U, Gibbs ZM, Li G, Bajaj S, et al. Computational and experimental investigation of TmAgTe$_2$ and XYZ$_2$ compounds, a new group of thermoelectric materials identified by first-principles high-throughput screening. J Mater Chem C 2015;3(40):10554–65.

[43] Alberi K, Nardelli MB, Zakutayev A, Mitas L, Curtarolo S, Jain A, et al. The 2019 materials by design roadmap. J Phys D Appl Phys 2019;52(1):013001.

[44] Agapito LA, Fornari M, Ceresoli D, Ferretti A, Curtarolo S, Nardelli MB. Accurate tight-binding Hamiltonians for two-dimensional and layered materials. Phys Rev B 2016;93(12):125137.

[45] Giannozzi P, Baroni S, Bonini N, Calandra M, Car R, Cavazzoni C, et al. Quantum ESPRESSO: a modular and open-source software project for quantum simulations of materials. J Phys Condens Matter 2009;21(39):395502.

[46] Giannozzi P, Andreussi O, Brumme T, Bunau O, Buongiorno Nardelli M, Calandra M, et al. Advanced capabilities for materials modelling with Quantum Espresso. J Phys Condens Matter 2017;29(46):465901.

[47] Supka AR, Lyons TE, Liyanage L, D'Amico P, Al Rahal Al Orabi R, Mahatara S, et al. AFLOWπ: a minimalist approach to high-throughput ab initio calculations including the generation of tight-binding Hamiltonians. Comput Mater Sci 2017;136:76–84.

[48] Agapito LA, Curtarolo S, Nardelli MB. Reformulation of DFT + U as a pseudohybrid hubbard density functional for accelerated materials discovery. Phys Rev X 2015;5(1):011006.

[49] Gopal P, Fornari M, Curtarolo S, Agapito LA, Liyanage LSI, Nardelli MB. Improved predictions of the physical properties of Zn- and Cd-based wide band-gap semiconductors: a validation of the ACBN0 functional. Phys Rev B 2015;91(24):245202.

[50] Lee S, Wang H, Gopal P, Shin J, Jaim HMI, Zhang X, et al. Systematic band gap tuning of BaSnO$_3$ via chemical substitutions: the role of clustering in mixed-valence perovskites. Chem Mater 2017;29(21):9378–85.

[51] Gopal P, De Gennaro R, Gusmao MSDS, Al Rahal Al Orabi R, Wang H, Curtarolo S, et al. Improved electronic structure and magnetic exchange interactions in transition metal oxides. J Phys Condens Matter 2017;29(44):444003.

[52] Dal Corso A. Pseudopotentials periodic table: from H to Pu. Comput Mater Sci 2014;95:337–50.

[53] Nardelli MB, Cerasoli FT, Costa M, Curtarolo S, De Gennaro R, Fornari M, et al. PAOFLOW: a utility to construct and operate on ab initio Hamiltonians from the projections of electronic wavefunctions on atomic orbital bases, including characterization of topological materials. Comput Mater Sci 2018;143:462–72.

[54] Hirao K. Analytic derivative theory based on the Hellmann–Feynman theorem. Can J Chem 1992;70(2):434–42.

[55] Yates JR, Wang X, Vanderbilt D, Souza I. Spectral and Fermi surface properties from Wannier interpolation. Phys Rev B 2007;75(19):195121.

[56] Arfken GB, Weber HJ. Mathematical methods for physicists. 6th ed. Boston: Elsevier; 2005.

[57] Goldstein H, Poole C, Safko J, Addison SR. Classical mechanics. Am J Phys 2002;70(7):782–3.

[58] Andrevv AA. The band edge structure of the IV–VI semiconductors. J Phys Colloq 1968;29(C4):C4-50–61.

[59] Vurgaftman I, Meyer JR, Ram-Mohan LR. Band parameters for III–V compound semiconductors and their alloys. J Appl Phys 2001;89(11):5815–75.

[60] Resca L, Mecholsky NA, Pegg IL. Band warping, band non-parabolicity, and Dirac points in electronic and lattice structures. Phys B 2017;522:66–74.

[61] Lavasani A, Bulmash D, Sarma SD. Wiedemann–Franz law and Fermi liquids. Phys Rev B 2019;99(8):085104.

[62] Transtrum MK, Qiu P. Model reduction by manifold boundaries. Phys Rev Lett 2014;113(9):098701.